The Meteoritical Society

Meteoritics & Planetary Science 57, Nr 1, 105–121 (2022)
doi: 10.1111/maps.13776

Unique igneous textures and shock metamorphism of the Northwest Africa 7203 angrite: Implications for crystallization processes and the evolutionary history of the angrite parent body

Hideyuki HAYASHI*[1], Takashi MIKOUCHI[2], Nak Kyu KIM[3], Changkun PARK[3], Yuji SANO[4,5], Atsushi TAKENOUCHI[6,7], Akira YAMAGUCHI[6], Hiroyuki KAGI[8], and Martin BIZZARRO[9]

[1]Department of Earth and Planetary Science, Graduate School of Science, The University of Tokyo, 7-3-1 Hongo, Bunkyo-ku, Tokyo 113-0033, Japan
[2]The University Museum, The University of Tokyo, 7-3-1 Hongo, Bunkyo-ku, Tokyo 113-0033, Japan
[3]Division of Earth Sciences, Korea Polar Research Institute (KOPRI), 26 Songdomirae-ro, Yeonsu-gu, Incheon 21990, Korea
[4]Atmosphere and Ocean Research Institute (AORI), The University of Tokyo, 5-1-5 Kashiwanoha, Kashiwa-shi, Chiba 277-8564, Japan
[5]Center for Advanced Marine Core Research, Kochi University, Monobe, Nankoku, Kochi B200,783-8502, Japan
[6]Antarctic Meteorite Research Center, National Institute of Polar Research (NIPR), 10-3 Midori-cho, Tachikawa, Tokyo 190-8518, Japan
[7]The Kyoto University Museum, Kyoto University, Yoshida-Honmachi, Sakyo-ku, Kyoto 606-8501, Japan
[8]Geochemical Research Center, Graduate School of Science, The University of Tokyo, 7-3-1 Hongo, Bunkyo-ku, Tokyo 113-0033, Japan
[9]Centre for Stars and Planet Formation, Globe Institute, University of Copenhagen, ØsterVoldgade 5-7, Copenhagen DK-1350, Denmark
*Corresponding author. E-mail: h.hayashi@eps.s.u-tokyo.ac.jp

(Received 25 March 2021; revision accepted 18 November 2021)

Abstract–Northwest Africa (NWA) 7203 is a quenched angrite, showing mineralogical features typically not present in other quenched angrites. NWA 7203 exhibits textures whose grain size varies from fine grains (<10 μm) to coarse grains (~3 mm), while other quenched angrites show only single-sized textures. Fine-grained and coarse-grained lithologies have nearly the same bulk compositions. Cooling rates were estimated to be ~80 °C h^{-1} for fine-grained lithologies and ~1 °C h^{-1} for coarse-grained lithologies. Mg-rich olivines (~Fo_{64}) were found only in fine-grained lithologies. Crystallization of NWA 7203 started in the fine-grained lithologies with Mg-rich olivine grains acting as seeds for crystallization. Coarse-grained lithologies were subsequently formed under conditions of slower cooling. NWA 7203 shows clear shock metamorphic textures unlike other quenched angrites except for NWA 1670. We confirm that the oxygen isotopic ratios of NWA 7203 plot on the angrite fractionation line within uncertainty. However, the obtained Pb-Pb age of NWA 7203 is 4543 ± 19 Ma, younger than the ages of other quenched angrites, which might be a result of disturbance by shock metamorphism. The finding of shock metamorphism of NWA 7203 suggests that some angrites might be derived from asteroids that remained large (>10 km in diameter) during the late heavy bombardment.

INTRODUCTION

Angrites are derived from a differentiated body and have crystallization ages ranging from 3 to 10 million years (Ma) after the formation of calcium-aluminum-rich inclusions (CAIs) (e.g., Amelin, 2008a; Kleine et al., 2012; Schiller et al., 2015). Angrites are basaltic achondrites that are depleted in volatile elements and enriched in refractory elements. Most angrites show either quenched or slowly cooled textures, with

quenched angrites having older crystallization ages compared with the slowly cooled angrites. For example, Pb-Pb ages of quenched angrites are 4562.4 ± 1.6 Ma for Asuka-881371, 4563.49 ± 0.20 Ma for D'Orbigny, and 4564.86 ± 0.38 Ma for Sahara 99555 (Amelin, 2008b; Tissot & Dauphas, 2012; Zartman et al., 2006), and those of slowly cooled angrites are 4556.44 ± 0.30 Ma for Angra dos Reis and 4558.55 ± 0.15 Ma for LEW 86010 (Amelin, 2008a; Tissot & Dauphas, 2012). Quenched angrites usually show diabasic textures and often include dendritic intergrowths consisting of olivine and anorthite. Slowly cooled angrites show granular textures.

When taking paired samples into consideration, 21 angrites are known as of October 2021 (The Meteoritical Bulletin Database). Among them, the quenched angrites are Asuka-881371 and its pair Asuka 12209, D'Orbigny, Lewis Cliff (LEW) 87051, Northwest Africa (NWA) 1296, NWA 1670, NWA 7203, NWA 7812, NWA 12004, NWA 12320, NWA 12774, NWA 12879, NWA 12934, NWA 13363, and Sahara 99555. Quenched angrites crystallized at fast cooling rates (e.g., Mikouchi et al., 1996). In addition, angrites almost universally lack shock metamorphism (e.g., Keil, 2012). The characteristics of fast cooling rates and lack of shock metamorphism make quenched angrites good time anchors (Brennecka & Wadhwa, 2012; McKeegan & Davis, 2003). Scott and Bottke (2011) considered that angrite parent body was at least 100 km in diameter and probably closer to Vesta in size. However, the absence of shock metamorphism in angrites led them to suggest that angrites are derived from asteroids that were small, that is, <10 km in diameter, and therefore survived the period of late heavy bombardment (LHB) without significant impact disruption. They proposed that a major impact on the angrite parent body occurred ~4.5 Gyr ago, producing angritic asteroids.

The NWA 1670 quenched angrite is known to show some evidence for shock metamorphism (Mikouchi et al., 2003). Our preliminary report also revealed that the NWA 7203 quenched angrite shows remarkable shock metamorphism (Hayashi et al., 2018). The discovery of these two shocked quenched samples among the total of 13 quenched angrites shows that it may be possible to use shocked angrites to infer whether angrites were already small asteroids or not during the timing of the LHB, as suggested by Scott and Bottke (2011).

Quenched angrites often contain Mg-rich olivine xenocrysts. Jambon et al. (2008) suggested that olivine xenocrysts are remnants of shock melting because most olivine xenocrysts in NWA 1670 are fractured and show mosaicism while some are characterized by faint undulatory extinction. Therefore, those olivine xenocrysts may also be evidence for shock metamorphism.

In order to better understand the formation history of the angrite parent body (APB) and to test the use of quenched angrites as a time anchor, it is important to study the mineralogy and petrology of shocked quenched angrites. Thus, in this work, we report on the petrology, mineralogy, and isotope systematics of the NWA 7203 angrite, which shows unique igneous and shock metamorphic textures, and discuss crystallization processes and the evolutionary history of the APB.

SAMPLE AND METHODS

NWA 7203 was found as a single stone with a total mass of 107 g in Morocco. A preliminary study identified it as a quenched angrite based on its texture and mineralogy (Mikouchi & Bizzarro, 2012).

We studied a slice of NWA 7203 (~4 cm × 4 cm × 3 mm) and made a thin section to perform a detailed mineralogical and petrological study. The thin section was analyzed by an optical microscope and by backscattered electron (BSE) imaging using a field emission electron probe micro analyzer (FE-EPMA, JEOL JXA-8530F, Department of Earth and Planetary Science, Graduate School of Science, The University of Tokyo). Mineral compositions and X-ray elemental maps were also acquired by FE-EPMA. Analytical conditions for quantitative wavelength-dispersive X-ray spectroscopy (WDS) analysis by FE-EPMA were 20 kV, 12 nA, and a 1 μm-sized beam, with counting times of 30 s on peaks and 15 s at the background positions, respectively. Well-characterized natural and synthetic materials were used for the standards. ZAF corrections were employed for quantitative analysis. X-ray elemental mapping was conducted by WDS at 15 kV accelerating voltage and 60 nA beam current. Selected elements are Si, Al, Ti, Fe, Mg, Ca, Na, K, Cr, and Ni. X-ray maps of the whole area of the thin section (approximately 15 mm × 20 mm), fine-grained lithology (1.5 mm × 1.5 mm), and coarse-grained lithology (2.1 mm × 2.1 mm) were obtained. To obtain modal abundances, we processed the X-ray maps using ImageJ. Threshold values were manually chosen to distinguish different mineral phases. Pixel counting was automated by ImageJ. Modal abundances of anorthite and pyroxene were obtained from the Al X-ray map. Anorthite is the most Al-rich phase. Pyroxene is the second-most Al-rich phase. Ulvöspinel contains approximately the same amount of Al as pyroxene, but ulvöspinel was distinguished and excluded using the Ti X-ray map. The modal abundance of olivine (including kirschteinite) was obtained from the Si X-ray map. The Si content of olivine is lower than those of anorthite and pyroxene, and higher than those of all other phases.

We obtained Raman spectra of minerals and glasses using a micro Raman spectrometer consisting of a 50 cm single polychromator (500is Imaging Spectrograph, Chromex) and an Si-based charge coupled device camera (DU-401A-BR-DD) at Geochemical Research Center, Graduate School of Science, the University of Tokyo and JASCO NRS-1000 Raman microscope at National Institute of Polar Research, Tokyo (NIPR). The excitation laser wavelength was 514.5 nm (500is Imaging Spectrograph) and 531.9 nm (JASCO NRS-1000), respectively. The laser power was 5 mW for 500is Imaging Spectrograph and 25 mW for JASCO NRS-1000. Wave number calibration was performed using naphthalene for 500is Imaging Spectrograph and silicon for JASCO NRS-1000, respectively.

Oxygen isotope ratios were measured using the three-oxygen isotope analytical system consisting of a CO_2 laser-BrF_5 fluorination system and a gas source isotope ratio mass spectrometer (IRMS, MAT 253 plus, Thermo Fisher Scientific) at Korea Polar Research Institute (KOPRI). An overview of the instrument is detailed in Kim et al. (2019, 2020). The instrument mainly consists of a reaction chamber, a purification line, and an IRMS. Approximately 2 mg of sample was placed in the reaction chamber, which is then filled with BrF_5. Fluorination was assisted by irradiation with a 25 W CO_2 laser with a wavelength of 10.6 μm by gradually increasing the lasing power. Isotopic ratio of purified oxygen gas (O_2) was measured using the IRMS. Data reproducibility was confirmed by measuring laboratory standard obsidians before and after sample measurements. We measured 2.09 mg of the fine-grained lithology of NWA 7203, and 2.31 and 2.57 mg of the coarse-grained lithology of NWA 7203. The yield of oxygen obtained from the samples was 94–96%.

Oxygen isotopic data are conventionally reported relative to VSMOW (Vienna Standard Mean Ocean Water reference material) using the delta (δ) notation: $\delta^i O = ([^iO/^{16}O]_{sample}/[^iO/^{16}O]_{VSMOW}) - 1$, where $i = 17$ or 18. We calibrated our working standard O_2 gas by comparing its oxygen isotope ratios with those of O_2 prepared by direct fluorination of VSMOW and SLAP (Standard Light Antarctic Precipitation) water standards with the same analytical system (Kim et al., 2020). We used SMOW-SLAP-normalized δ-values to get $\Delta'^{17}O$, the deviation of the $^{17}O/^{16}O$ ratio from the reference fractionation line defined by $\Delta'^{17}O = \ln(1 + \delta^{17}O_{normalized}) - \lambda_{RL} \times (1 + \delta^{18}O_{normalized}) - \gamma_{RL}$, where λ_{RL} is the slope of the reference fractionation line in the linearized three-oxygen isotope plot and γ_{RL} is a y-axis offset of the line. We used λ_{RL} of 0.5278 and γ_{RL} of −0.040‰ (Kim et al., 2020).

Pb-Pb dating of NWA 7203 was carried out by measuring Pb isotope ratios of silico-apatites in the polished thick section using the Nano-SIMS at Atmosphere and Ocean Research Institute, the University of Tokyo (Koike et al., 2014). Measurement conditions were 300 pA for primary ions and $^{16}O^-$ for ion sources. Pre-sputtering was performed for 8 min in the range of 10 × 10 μm. In the SIMS measurement, raster diameters of 3 × 3 μm and analysis time of 60 s were applied for two magnetic fields, respectively, and repeated for 30 cycles. Analytical area (3 × 3 μm) is divided into 32 × 32 pixels (~0.1 × 0.1 μm for each pixel), and the counts of each mass number were obtained for each pixel. For the standard, NIST SRM 610 was used. Total measurement time was 1 hour per point. We measured signals of ^{31}P, ^{44}Ca, ^{204}Pb, ^{206}Pb, ^{207}Pb, ^{238}UO, $^{238}UO_2$, ^{31}P. We checked ^{44}Ca to confirm whether silico-apatite was successfully measured or not. We rejected the data for any pixels counting less than half of the maximum pixel of ^{31}P in the cycle. In addition, the data with the high ^{204}Pb counts (these data are found only in the early cycles and the ^{204}Pb counts decrease exponentially with each cycle due to sputtering) were also rejected because they were considered to reflect terrestrial contamination on the surface. Pb/U ratios could not be determined because a suitable matrix-matched standard of silico-apatite was not available.

RESULTS

Petrography of Igneous Textures

The NWA 7203 slice used for this study clearly exhibits two distinct lithologies with different grain sizes (Fig. 1a). Accordingly, textures of NWA 7203 can be divided into "fine-grained" and "coarse-grained" lithologies. Grain sizes of fine-grained lithologies range from several to a few hundred μm, and those of coarse-grained lithologies range up to 2 mm. Optical microscope observations show that a variolitic texture extends radially from fine-grained lithologies to coarse-grained lithologies (Fig. 1b). Coarse-grained lithologies appear to grow from variolitic fine-grained lithologies as seeds, and grain size gradually changes at the 1–2 mm boundary of distance between fine-grained and coarse-grained lithologies. Coarse-grained lithologies appear to fill gaps between fine-grained lithologies. Areas of coarse-grained lithologies are slightly more abundant (volumetrically) than fine-grained lithologies in the slice that we studied. Both fine-grained and coarse-grained lithologies of NWA 7203 mainly consist of olivine and kirschsteinite, Al-Ti-rich clinopyroxene, and pure anorthite, with accessory ulvöspinel, troilite, and silico-apatite. Hercynite is a rare component in coarse-grained lithologies. Fine-grained lithologies show a variolitic

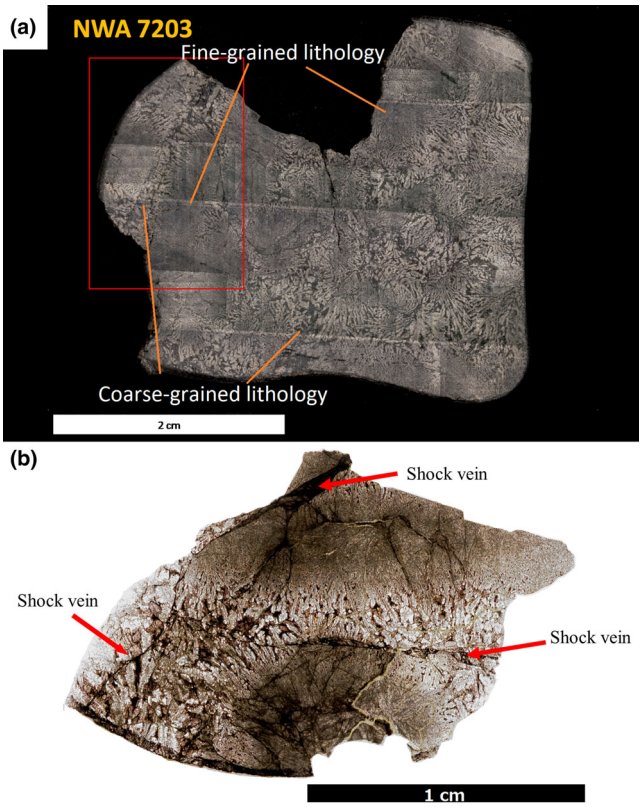

Fig. 1. Studied slice and thin section of NWA 7203. a) 3 mm thick slice with ~4 × 4 cm dimensions. The thin section was prepared from the rectangular area shown in the image. b) Optical photomicrograph of the NWA 7203 thin section (open Nicol). A black shock vein near the top of the thin section has the largest width (about 600 μm). (Color figure can be viewed at wileyonlinelibrary.com.)

texture reaching about 1 cm in size, and have rounded outlines (Fig. 2a). In this lithology, anorthite grains are lath shaped with parallel arrangement, and olivine and clinopyroxene are interstitial to the elongated anorthite grains (Fig. 2b). Accessory minerals such as troilite and ulvöspinel (several μm in size) are also present. In the fine-grained lithology nearing the boundary with the coarse-grained lithology, olivine also occurs as elongated grains parallel to the direction of the elongation of anorthite grains. Approaching the coarse-grained lithologies, olivine grain size gradually increases and then begins to show dendritic textures consisting of olivine and anorthite to form the boundary against the coarse-grained lithologies (Fig. 2c).

In the coarse-grained lithologies, olivine and anorthite form dendrites, and clinopyroxene fills the gap between dendrites (Fig. 2d). The dendrites gradually become coarse-grained moving away from the variolitic fine-grained lithologies. In some areas, olivine and anorthite form graphic textures. Accessory minerals such as troilite and ulvöspinel often occur near the Fe-rich olivine. Silico-apatite occurs as inclusions in clinopyroxene or near troilite and ulvöspinel assembly. Silico-apatite grains show a euhedral shape or in some places occur in clinopyroxene as lamellar shape inclusions. The sizes of troilite, ulvöspinel, and silico-apatite are usually tens of μm in coarse-grained lithologies, but troilite can range up to several hundred μm. Hercynite is rare and occurs as inclusion in clinopyroxene with the size of ~10 μm.

Bulk Chemical Composition

We performed 16 × 16 point grid analysis three times each for fine- and coarse-grained lithologies with FE-EPMA to obtain bulk compositions. Mean values of the grid analyses are interpreted to reflect the bulk composition of each lithology. The bulk composition of the fine-grained lithologies is estimated to be SiO_2 = 40.4 ± 0.6 wt%, Al_2O_3 = 15.3 ± 0.4 wt%, TiO_2 = 0.89 ± 0.05 wt%, FeO = 21.7 ± 1.0 wt%, MgO = 6.3 ± 0.3 wt%, CaO = 15.5 ± 0.3 wt%, Cr_2O_3 = 0.07 ± 0.01 wt%, and total = 100.4 ± 0.1 wt%, and that of the coarse-grained lithologies is estimated to be SiO_2 = 40.6 ± 0.3 wt%, Al_2O_3 = 14.7 ± 0.4 wt%, TiO_2 = 0.7 ± 0.1 wt%, FeO = 21.9 ± 0.4 wt%, MgO = 7.7 ± 0.7 wt%, CaO = 14.6 ± 0.3 wt%, Cr_2O_3 = 0.08 ± 0.01 wt%, and total = 100.57 ± 0.7 wt% (all errors are shown in 1SD). We define Mg# as molar (Mg/[Mg+Fe^{2+}] × 100), and Mg# of fine-grained lithologies is 34 ± 1 and Mg# of coarse-grained lithologies is 38 ± 4, respectively.

Modal Abundances of Minerals and Mineral Compositions

Modal Abundance

Modal abundance was estimated by elemental X-ray maps. The modal abundances of constituent minerals of NWA 7203 were estimated to be olivine = 41 vol%, clinopyroxene = 24 vol%, and anorthite = 34 vol%. The modal abundances of minerals in the fine-grained lithology were estimated to be olivine = 36 vol%, clinopyroxene = 30 vol%, and anorthite = 33 vol%. Modal abundance of the coarse-grained lithology was olivine = 38 vol%, clinopyroxene = 23 vol%, and anorthite = 37 vol%. Note that the modal abundance estimates are uncertain for two reasons. The raw data of the elemental X-ray maps have value blur. In addition, the spatial resolution of the maps is only 3 μm per pixel. Thus, the pixel value sometimes reflects more than one phase; this effect is especially significant for fine-grained lithologies. Thus, it is not possible to determine universal uncertainties for the modal abundances, but we estimate that they are several %.

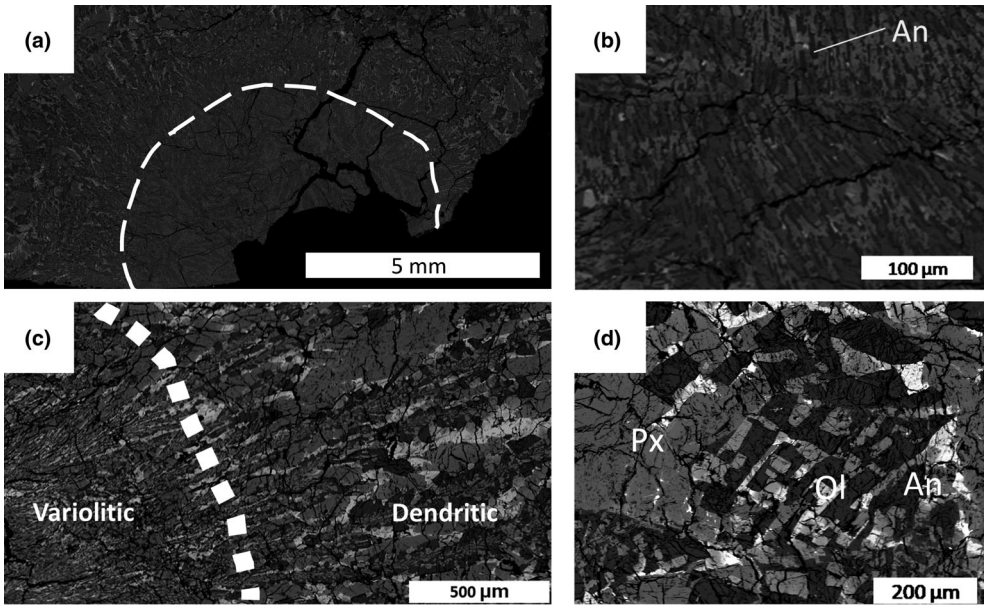

Fig. 2. BSE images showing igneous textures of NWA 7203. a) Large-scale BSE image of NWA 7203. Fine-grained lithology shows a variolitic texture (surrounded by a dotted line). b) BSE image of the fine-grained lithology, showing that olivine and clinopyroxene fill the gap of elongated anorthite. c) BSE image of the boundary of variolitic fine-grained lithology and dendritic coarse-grained lithology. d) BSE image of the coarse-grained lithology. In coarse-grained lithologies, olivine and anorthite form dendrites, and clinopyroxene fills the gaps between the dendrites.

Olivine

Olivine in NWA 7203 shows chemical zoning that is similar to that in other quenched angrites. To describe the olivine chemical compositions, we define Fo# as mole percent of Mg/(Mg + Fe + Ca), Fa# as mole percent of Fe/(Mg + Fe + Ca), and La# as mole percent of Ca/(Mg + Fe + Ca), respectively. Olivine and kirschsteinite exist both in the fine-grained and coarse-grained lithologies. Typically, dendritic olivine in coarse-grained lithologies shows strong chemical zoning from Mg-rich interiors to more Fe-rich edges that transition to kirschsteinite. From interior to edge of olivine, chemical compositions first change typically from $Fo_{40}Fa_{56}La_4$ to $Fo_{14}Fa_{76}La_{10}$, then the phase jump into the kirschsteinite, and finally chemical compositions change from $Fo_5Fa_{63}La_{32}$ to $Fo_0Fa_{80}La_{20}$. In Fig. 3, we plotted the olivine composition of both fine-grained and coarse-grained lithologies. The olivine compositions in NWA 7203 are broadly consistent with the phase equilibrium relationships of Ca-Mg-Fe olivine at around 800–1000 °C (Davidson & Mukhopadhyay, 1984) (shown in Fig. 3). Olivine in the coarse-grained lithologies is $Fo_{59–0}$ while that in the fine-grained lithologies is $Fo_{64–4}$ (mostly $Fo_{54–4}$). The average composition of olivine was estimated from olivines randomly chosen by grid analysis (Table 1).

From the Mg X-ray map, we found that occasionally there are Mg-rich olivine grains ($Fo_{60–64}$) only near the center of the fine-grained lithologies

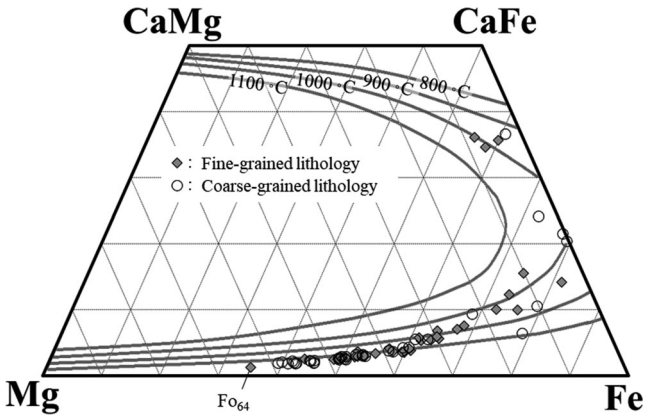

Fig. 3. Chemical compositions of olivine and kirschsteinite in NWA 7203. Phase equilibrium relationships of Ca-Mg-Fe olivine at 800–1100 °C (Davidson & Mukhopadhyay, 1984) are also shown.

(Fig. 4) with compositions that are up to Fo_{64}, although most olivine in the fine-grained lithologies of NWA 7203 is $Fo_{\leq 54}$. The most Mg-rich olivine grain (Fo_{64}) is characterized by a blade-shaped growth texture (~1 mm long and ~20 µm wide) intergrown with anorthite, showing growth from the Mg-rich olivine core (Fig. 5). Elongated anorthites grow perpendicular to this Mg-rich olivine blade as a seed. Optical observations indicate that the core of this Mg-rich olivine is a single crystal, and a size is about 100 µm × 50 µm, which is

Table 1. Chemical composition of olivine. Olivine shows strong chemical zoning.

	Olivine							
	Mg-rich olivine core	Mg-rich olivine rim	Fine phenocryst olivine (Mg-rich)	Fine phenocryst olivine (Fe-rich)	Coarse phenocryst olivine (Mg-rich)	Coarse phenocryst olivine (Fe-rich)	Average fine olivine (N = 17)	Average coarse olivine (N = 44)
SiO_2	37.6	33.7	35.8	33.3	36.6	31.7	34.6	35.1
Al_2O_3	0.16	0.09	0.05	0.06	0.07	0.02	0.2	0.2
TiO_2	0.06	0.07	0.05	0.07	0.01	0.08	0.1	0.1
FeO	29.9	49.9	38.1	54.2	35.1	57.4	44.8	42.8
MnO	0.40	0.72	0.59	0.80	0.45	0.98		
MgO	31.5	12.2	24.1	7.65	27.4	0.75	17.0	19.0
CaO	0.79	3.77	1.61	4.64	1.13	8.60	3.5	3.6
Na_2O	n.d.	n.d.	0.04	n.d.	0.03	0.05	0.1	0.1
K_2O	n.d.	0.00	0.02	0.00	n.d.	n.d.	0.0	0.0
Cr_2O_3	0.11	0.01	0.11	0.01	0.03	n.d.	0.1	0.1
NiO							0.0	0.0
Total	100.5	100.4	100.4	100.7	100.9	99.5	100.3	100.8
Fo#	64.5	28.4	51.7	18.5	57.2	1.9	38.1	41.7

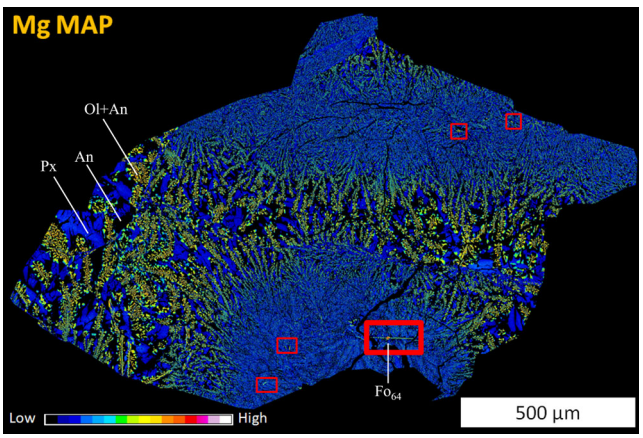

Fig. 4. Mg X-ray map of NWA 7203. Warm color indicates high concentration of Mg. There are several Mg-rich grains near the center of the fine-grained lithologies (inside of red squares). The most Mg-rich olivine grain in this thin section exists inside of the red bolded square. (Color figure can be viewed at wileyonlinelibrary.com.)

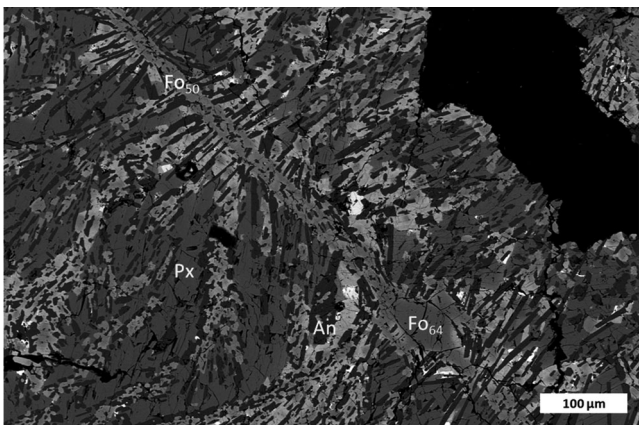

Fig. 5. BSE image of the most Mg-rich olivine grain. The core part has an Mg-rich chemical composition reaching Fo_{64}.

larger than the surrounding olivines. Minor elements in the Mg-rich olivine core are CaO = 0.9 wt% and Cr_2O_3 = 0.1 wt%, while those of other olivines in the fine-grained lithologies are CaO = 3.5 wt% and Cr_2O_3 = 0.1 wt%.

Clinopyroxene

Clinopyroxene in NWA 7203 also shows extensive chemical zoning similar to that in other quenched angrites. Chemical compositions of clinopyroxene range from $Fs_{33}En_{15}Wo_{52}$ to $Fs_{46}En_{0}Wo_{54}$ in the coarse-grained lithologies, and $Fs_{24}En_{21}Wo_{55}$ to $Fs_{37}En_{12}Wo_{51}$ in the fine-grained lithologies. Mg# versus CaO (wt%) for the pyroxene are shown in Fig. 6. Clinopyroxene contains 5–10 wt% Al_2O_3, 1–7 wt% TiO_2, and 0.0–0.5 wt% Cr_2O_3. The average composition of clinopyroxene was estimated from clinopyroxenes randomly chosen by grid analysis (Table 2).

Anorthite

The chemical composition of anorthite is homogeneous ($An_{>99.5}$) both in fine-grained and coarse-grained lithologies. It contains ~1 wt% FeO.

Accessory Minerals

Troilite and ulvöspinel have constant chemical compositions. Silico-apatites contain 11–22 wt% of SiO_2. Hercynite has composition $(Fe^{2+}_{0.68–0.71}, Mg_{0.32–0.29})(Al_{1.25–1.17}, Cr_{0.61–0.69}, Fe^{3+}_{0.10–0.09}, Ti^{4+}_{0.04–0.05})O_4$.

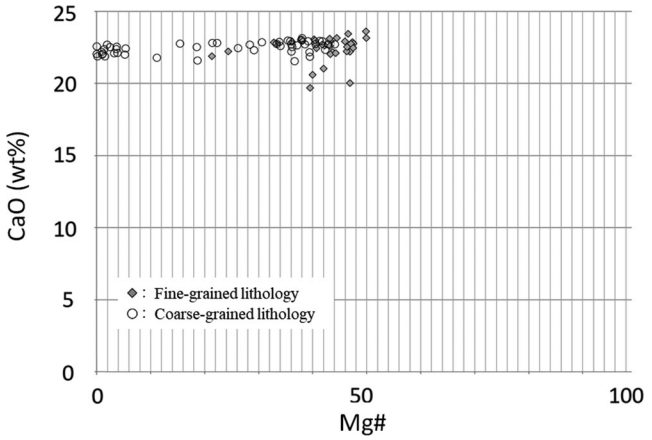

Fig. 6. Chemical compositions of clinopyroxene in NWA 7203. Mg# of clinopyroxene is 0–44 in coarse-grained lithologies and 24–50 in fine-grained lithologies, respectively.

Chemical compositions of constituent minerals in NWA 7203 are summarized in Tables 1–3.

Petrography of Shock Textures

Shock melt veins are pervasive in the thin section studied. In the fine-grained lithology, there are many thin (about several μm wide) shock veins whereas in the coarse-grained lithology, there are only a few thick (about 100 μm wide) shock veins (Fig. 1b). Around the shock veins, some olivine, anorthite, and clinopyroxene show undulose extinction from optical microscopic observations. It is difficult to determine whether anorthites near the shock veins are crystalline or amorphous under optical microscope because the areas are darkened. In some parts, shock veins cut pre-existing igneous textures. For example, Fig. 7a shows the displacement of the assembly of Fe-rich olivine and troilite (displacement size: ~1 mm). The maximum width of the shock vein in the studied thin section is up to 600 μm. The rims of the vein are typically 100 μm wide and glassy. Between two glassy rims, variolitic assemblages are brecciated (Fig. 7b). Shock veins with width of around 100 μm are composed of glass, fragments of pre-existing minerals, and recrystallized clinopyroxenes with a maximum size of 10 μm (Figs. 7c and 7d). These clinopyroxene grains are more Al-rich (Al_2O_3 = 10–13 wt%) and Ca-depleted (CaO = 14–18 wt%) than those outside the shock melt veins. From Raman spectrum, we confirmed that recrystallizing clinopyroxene is a crystalline pyroxene phase (Fig. 8a). Because Al-rich pyroxene in shock veins has been reported to be a high-pressure phase in some meteorites (e.g., Ma & Beckett, 2017), the recrystallized pyroxene in NWA 7203 may be a high-pressure phase. Anorthite about 10 μm away from the glassy shock vein is amorphous as indicated by broad Raman peaks (Fig. 8b).

Oxygen Isotopic Ratios

Oxygen isotope results are shown in Table 4. In order to compare our oxygen isotope results for NWA 7203 with data from other angrites, we plot our data with the previously reported data in Fig. 9. Since Greenwood et al. (2005) used 0.5247 as a slope (λ_{RL}) of the reference fractionation line and zero offset of the line, we recalculated our data with λ_{RL} of 0.5247 and γ_{RL} of zero. The average of recalculated $\Delta'^{17}O$ values for three measurement sessions of NWA 7203 in this study is -0.077 ± 0.015 (1σ), identical within errors with the value -0.072 ± 0.007 (1σ) from Greenwood et al. (2005). Thus, NWA 7203 is an angrite in terms of oxygen isotopic composition. The difference of $\delta^{18}O$ values was caused by mass dependent isotope fractionation for each phase (Clayton & Kieffer, 1991).

Pb-Pb Age

We measured Pb isotopes of ^{204}Pb, ^{206}Pb, and ^{207}Pb in silico-apatite, focusing on grains large enough to obtain accurate data. All silico-apatite grains measured in this study were located in coarse-grained lithologies. Silico-apatite grains show subhedral to euhedral shapes, and with sizes of 20–50 μm (Fig. 10). We measured Pb isotopic ratios once for each grain but measured several spots for larger (~50 μm) grains. Raw counts of each isotope are shown in Table 5. We show a $^{207}Pb/^{206}Pb$ versus $^{204}Pb/^{206}Pb$ isochron diagram in Fig. 11. All data points define a regression line corresponding to a Pb-Pb age of 4543 ± 19 Ma (2σ, MSWD = 2.0). Restricting our analysis to the silico-apatites located >200 μm from the thick (<50 μm) glassy shock veins yields a Pb-Pb age of 4561 ± 20 Ma (2σ, MSWD = 1.2). This age is indistinguishable from the Pb-Pb of 4555 ± 32 Ma defined by the silico-apatites located near (<200 μm) the shock veins (2σ, MSWD = 1.3).

DISCUSSION

Crystallization Process of NWA 7203

NWA 7203 exhibits the typical mineralogy and textures of quenched angrites except for the large variations of grain sizes and the existence of Mg-rich olivine crystals only in fine-grained lithologies. NWA 7203 has oxygen isotopic ratios corresponding to the angrite fractionation line (AFL), confirming that NWA 7203 is an angrite. It is important to clarify the crystallization history of this angrite in order to

Table 2. Chemical compositions of clinopyroxene. Clinopyroxene shows chemical zoning.

	Clinopyroxene					
	Fine phenocryst clinopyroxene (Mg-rich)	Fine phenocryst clinopyroxene (Fe-rich)	Coarse phenocryst clinopyroxene (Mg-rich)	Coarse phenocryst clinopyroxene (Fe-rich)	Average fine clinopyroxene (N = 36)	Average coarse clinopyroxene (N = 48)
SiO_2	47.7	45.4	45.9	44.6	46.0	44.7
Al_2O_3	5.59	4.70	7.77	4.07	8.3	7.7
TiO_2	1.49	2.60	2.01	1.47	2.2	2.8
FeO	16.0	24.9	15.9	29.1	15.3	20.0
MnO	0.25	0.26	0.17	0.31		
MgO	6.91	1.30	6.33	0.07	6.2	3.5
CaO	21.76	21.8	21.8	20.4	22.5	22.5
Na_2O	0.03	0.02	n.d.	0.00	0.0	0.1
K_2O	0.02	n.d.	0.01	n.d.	0.0	0.0
Cr_2O_3	0.15	0.01	0.46	n.d.	0.2	0.2
NiO					0.0	0.1
Total	99.9	101.0	100.4	100.0	100.8	101.3
Wo	49.6	50.6	50.7	47.2	52.3	52.4
En	21.9	4.2	20.5	0.2	20.0	11.3
Fs	28.5	45.2	28.8	52.6	27.7	36.3
Mg#	43.5	8.5	41.5	0.4	41.9	23.8

Table 3. Chemical compositions of anorthite, ulvöspinel, and silico-apatite.

	Anorthite		Ulvöspinel		Silico-apatite
	Fine anorthite	Coarse anorthite	Fine ulvöspinel	Coarse ulvöspinel	Coarse silico-apatite
SiO_2	44.1	44.5	0.25	0.30	12.4
Al_2O_3	36.7	36.8	1.66	4.10	0.36
TiO_2	0.01	0.06	31.4	25.4	1.51
FeO	1.20	0.56	64.1	67.1	5.24
MnO	0.02	0.02	0.41	0.41	0.04
MgO	0.17	0.22	0.07	0.01	0.03
CaO	19.5	19.4	0.61	0.67	48.6
Na_2O	0.09	0.06	0.01	n.d.	n.d.
K_2O	0.01	0.01	n.d.	0.01	0.01
Cr_2O_3	0.06	n.d.	0.03	n.d.	
P_2O_5					29.9
Total	101.8	101.7	98.6	98.0	98.9
An#	99.1	99.4			

understand the various crystallization processes that occurred on APB.

We first discuss the process that resulted in the spatial separation of the fine-grained and coarse-grained lithologies, which requires a comparison of the bulk composition and the chemical compositions of minerals in the two lithologies. The bulk compositions of fine-grained and coarse-grained lithologies obtained by the EPMA grid analyses are indistinguishable within analytical uncertainty. This result suggests that the crystallization of NWA 7203 proceeded nearly in situ, without significant fractional crystallization.

However, the chemical compositions of olivine and clinopyroxene are different in the two lithologies. The average chemical composition of olivine is more Mg-rich in the coarse-grained lithologies compared with that in the fine-grained lithologies (Table 1). The average chemical composition of clinopyroxene is more Mg-rich in the fine-grained lithologies compared to the coarse-grained lithologies (Table 2), which is opposite to the trend observed for olivine.

The chemical compositions of olivine and clinopyroxene in fine-grained and coarse-grained lithologies are complementary. In the fine-grained lithologies, olivine and clinopyroxene form a banded texture, while in the coarse-grained lithologies, dendrites crystallized first and clinopyroxene filled the gaps of dendrites. From these distinct chemical compositions

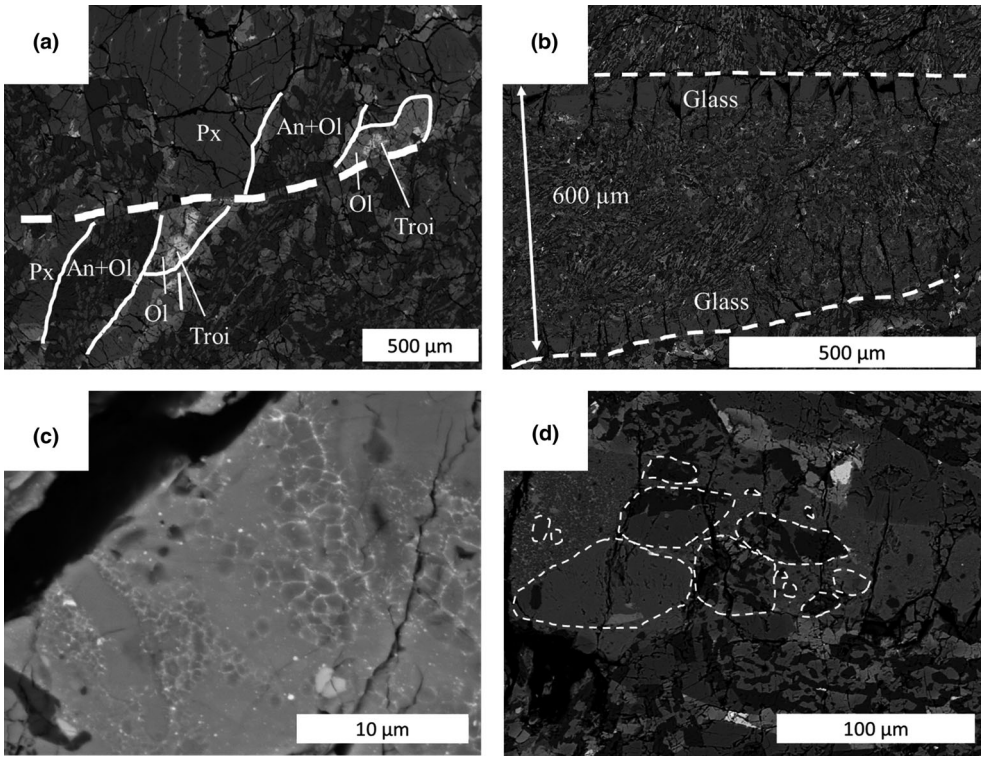

Fig. 7. Shock metamorphic textures found in NWA 7203. a) Pre-existing textures were displaced by 1 mm by the shock vein. b) Shock vein with the maximum width (around 600 µm) in this thin section (inside of the white dotted line). Both rims of the vein are glass, and between two glassy rims, dendritic textures are brecciated. c) Small clinopyroxenes crystallized from shock melt.d) Glassy shock vein and relict mineral fragments inside it.

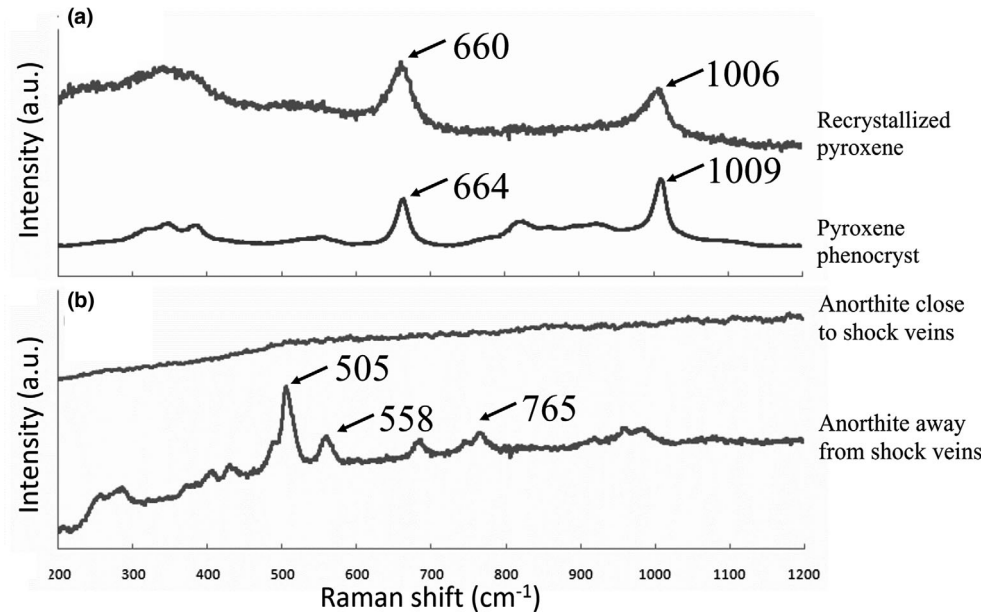

Fig. 8. a) Raman spectra of recrystallized pyroxene and pyroxene phenocryst. b) Raman spectra of anorthite close to shock veins and anorthite away from shock veins.

and textures, we propose different cooling rates in each lithology, resulting in differences of the degree of supercooling of the magma. In the coarse-grained lithologies, crystallization occurred under "near-equilibrium" conditions. Olivine and anorthite crystallized before the crystallization of clinopyroxene

Table 4. Oxygen isotopic ratios for each sample of NWA 7203, presented using VSMOW for reference. $\delta^{17}O$, $\delta^{18}O$, and $\Delta'^{17}O$ values are shown in ‰.

	Weight (mg)	$\delta^{17}O_{VSMOW}$‰ [a] (1σ)	$\delta^{18}O_{VSMOW}$‰ [a] (1σ)	$\Delta'^{17}O$‰ [b] (1σ)	$\Delta'^{17}O$‰ [c] (1σ)
NWA 7203_coarse_1	2.09	2.150 ± 0.042	4.239 ± 0.018	−0.044 ± 0.046	−0.072 ± 0.046
NWA 7203_coarse_2	2.31	2.183 ± 0.027	4.292 ± 0.014	−0.039 ± 0.024	−0.066 ± 0.024
NWA 7203_fine	2.53	2.091 ± 0.034	4.169 ± 0.012	−0.067 ± 0.033	−0.094 ± 0.033

[a]δ-values were applied on two-point scaling (VSMOW-SLAP scale). The oxygen isotope measurements of standard waters were performed in an identical purification line used for mineral analysis.
[b]To report the $\Delta'^{17}O$ value, we assigned the slope (λ) and y-intercept of mass dependent fractionation line as 0.5278 and −0.0402, respectively.
[c]Recalculated $\Delta'^{17}O$ values with a slope (λ) of 0.5247 and zero intercept for accurate comparison with previous data (Greenwood et al., 2005).

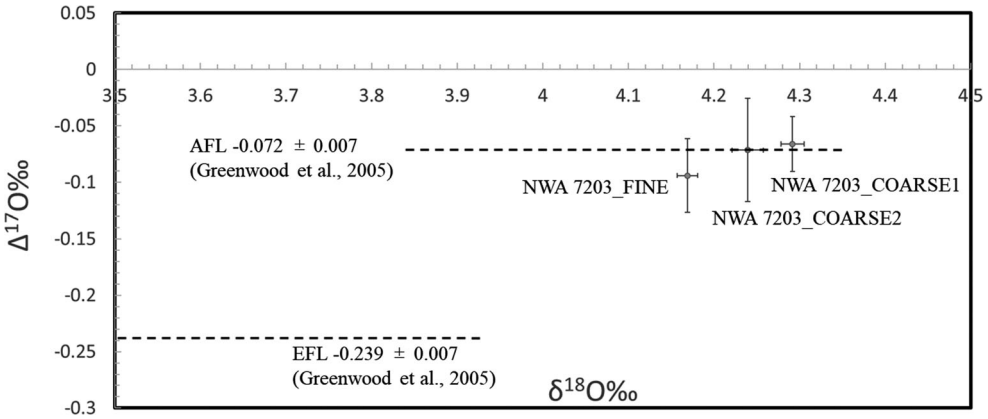

Fig. 9. $\Delta'^{17}O$ versus $\delta^{18}O$‰ for each sample of NWA 7203. $\Delta'^{17}O$ values are recalculated with a slope (λ) of 0.5247 and zero intercept for just comparison with previous data. AFL and eucrite fractionation line (EFL) values are from Greenwood et al. (2005).

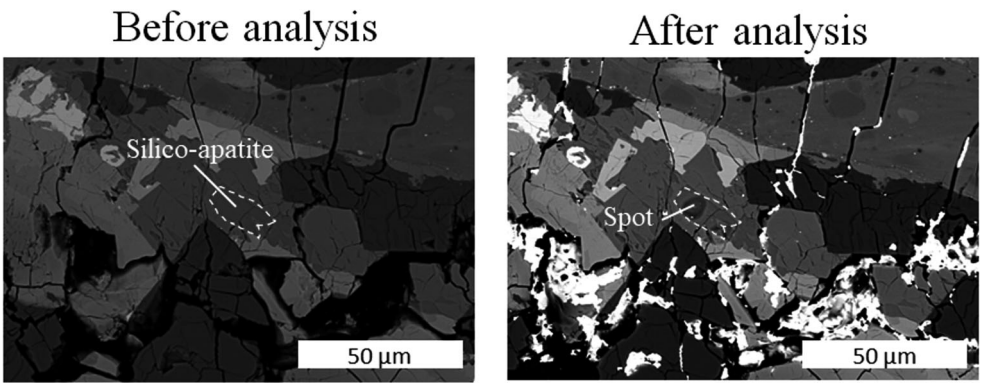

Fig. 10. BSE images of silico-apatite in NWA 7203 before and after nano-SIMS analysis. White irregular patches in the "after" figure are remnants of gold coating.

which corresponds to the phase diagram of an angritic system (Longhi, 1999), and Fo# of olivine was higher than that in the fine-grained lithologies. In contrast, the degree of supercooling was larger in the fine-grained lithologies. Olivine, clinopyroxene, and anorthite crystallized simultaneously and the Fo# of olivine decreased while the Mg# of clinopyroxene increased.

A key phase in NWA 7203 is the rare Mg-rich olivine crystals (up to Fo_{64}) only found in the fine-grained lithologies. If we consider the bulk chemical composition of the fine-grained lithology as estimated by EPMA grid analysis, the calculated Fo# crystallized from this bulk composition is $Fo_{61 \pm 3}$ (Roeder & Emslie, 1970). The Fo_{64} olivine appears to be in equilibrium with the bulk composition. Thus, these Mg-rich olivine grains are early phenocrysts. However, the Fo_{64} olivine is the largest grain in size in the fine-grained lithology and the most Mg-rich in comparison

Table 5. Raw counts of ^{206}Pb, ^{204}Pb, ^{207}Pb, and ^{44}Ca. When we calculate $^{204}Pb/^{206}Pb$ and $^{207}Pb/^{206}Pb$, we multiply ^{204}Pb by 1.204(2) and ^{207}Pb by 0.989(4).

	Total ^{206}Pb	Total ^{204}Pb	Total ^{207}Pb	Total ^{44}Ca
Grain1_1	832	10	549	21684059
Grain1_2	4927	102	3449	157477329
Grain1_3	3757	50	2659	160046901
Grain4	3258	56	2444	105711541
Grain6	5896	77	4032	97751119
Grain7_1	8295	31	5358	103583780
Grain7_2	6240	83	4394	49032337
Grain8	40852	99	25860	86405633
Grain9_1	17652	180	11620	130698636
Grain9_2	12569	203	8364	96407417
Grain9_3	4162	12	2707	58469814
Grain10	15408	110	10291	122273944

with olivines around it. It shows a homogeneous core composition, which is different from other fine-grained phenocrystic olivine grains in this lithology. Furthermore, it is texturally evident that fine-grained lithologies crystallized first and coarse-grained lithologies subsequently formed, because the NWA 7203 texture extends radially from fine-grained lithologies to coarse-grained lithologies and coarse-grained lithologies appear to fill the gaps between fine-grained lithologies. From the observation that Mg-rich olivine grains exist only in fine-grained lithologies, and anorthite grows on these olivine grains, we interpret the olivines to have acted as seeds. Such Mg-rich olivine as early phenocrysts exist in the "core" of the variolitic texture, indicating that the crystallization proceeded radially to form the variolitic textures of fine-grained lithologies.

Quenched angrites often contain Mg-rich olivine xenocrysts and those show evidence for atomic diffusion (e.g., Fe-Mg and Ca) related to the interaction with the surrounding melts, which can be used to estimate cooling rates (e.g., Mikouchi, McKay, & Le, 2000). Because the Fo_{64} olivine phenocrysts are considered to have crystallized first in NWA 7203 and have homogeneous core compositions, we can estimate the cooling rate of NWA 7203 in a similar manner. We calculated atomic diffusion profiles for cooling from 1200 to 900 °C at two log units above the iron–wüstite buffer (log fO_2 = IW+2; Jurewicz et al., 1993). Based on the Fe-rich bulk composition of angrite magmas (Mikouchi et al., 1994), we adopted a starting temperature of 1200 °C. We used a diffusion coefficient of Fe-Mg in olivine from Misener (1974) as demonstrated by Miyamoto et al. (2002). The best fit cooling rate obtained is 80 °C h^{-1} (Fig. 12).

We are not able to apply the same approach to estimate a cooling rate for the coarse-grained lithology because Mg-rich olivine xenocrysts or phenocrysts with homogeneous cores are absent in this lithology. Instead, we estimate the cooling rate using the textural characteristic of quenched angrites. Mikouchi, McKay, and Le (2000) reported that the 1 °C h^{-1} cooling crystallization experiment of the Asuka-881371 composition melt (1300−900 °C, logfO_2 = IW+2) produced a dendritic texture of olivine and anorthite similar to Sahara 99555 while faster cooling rates (5, 10, and 50 °C h^{-1}) did not crystallize anorthite. In the coarse-grained lithologies, such dendrites consisting of olivine and anorthite exist. Although kinetic issues control the textural variations, we consider that the cooling rate of the coarse-grained lithologies could be on the order of 1 °C h^{-1}.

The textural difference of NWA 7203 between fine-grained and coarse-grained lithologies could be caused by the difference of cooling rates. Namely, the fine-grained lithologies cooled faster, and then, subsequent crystallization of the coarse-grained lithologies took place under a relatively slower cooling condition, which is consistent with the estimated cooling rates of both lithologies (fine-grained: 80 °C h^{-1} versus coarse-grained: ~1 °C h^{-1}). One of the possible scenarios to explain the change of cooling rates from fast to slow is a lobe of quenching basalt overridden by a new breakout of lava from the main flow in a single eruption cycle. Alternatively, it is possible that the changing cooling rates may simply be a function of supercooling. Rapid cooling led to a supercooled state, during which time the early olivine phenocryst was modified by intracrystal diffusion at ~80 °C h^{-1}. Nucleation on the olivine phenocryst and rapid crystallization will generate fine-grained texture, which expels heat into the magma/bulk rock, resulting in slower cooling rate (~1 °C h^{-1}).

A schematic illustration of the crystallization process of NWA 7203 is shown in Fig. 13. Crystallization of NWA 7203 started with Mg-rich olivine grains as crystallization seeds at a relatively fast cooling rate (about 80 °C h^{-1}) and formed a fine-grained variolitic texture. Before completion of the crystallization process, the material was covered by a new lava flow resulting in an increased burial depth and, hence, a change toward slower cooling rates (~1 °C h^{-1}). Thus, final crystallization was completed at a slower cooling rate and produced a coarse-grained dendritic texture.

Comparison Between NWA 7203 and Other Quenched Angrites

NWA 7203 shows a variolitic texture in the fine-grained lithologies and dendritic texture in the coarse-

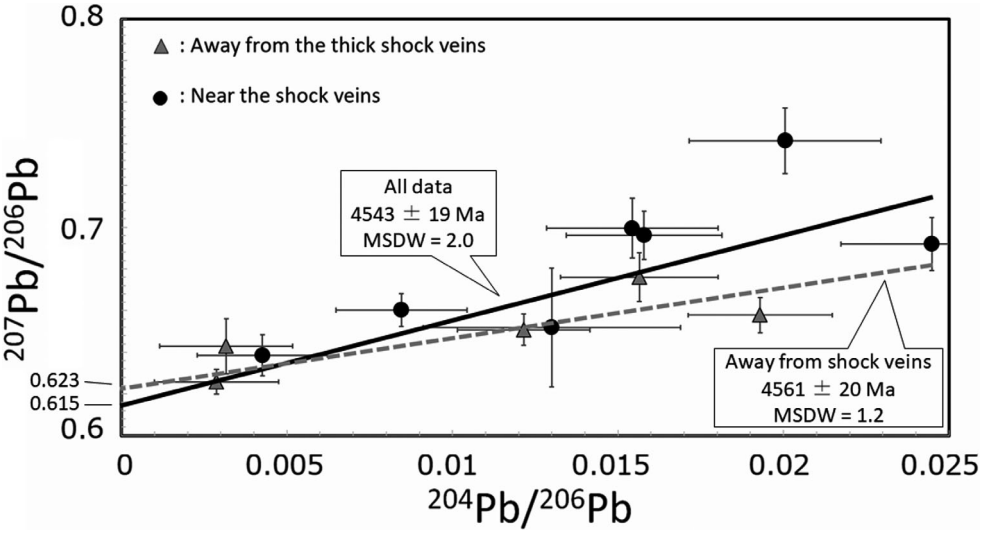

Fig. 11. $^{207}Pb/^{206}Pb$ versus $^{204}Pb/^{206}Pb$ for each point of silico-apatites in NWA 7203. The intercept value of the regression line estimated from a least-squares method corresponds to a Pb-Pb age. All data points define a regression line (shown in solid line) corresponding to a Pb-Pb age of 4543 ± 19 Ma (2σ, MSWD = 2.0), and data only for the silico-apatites located away (>200 μm) from the thick (<50 μm) glassy shock veins define a regression line (shown in dotted line) corresponding to a Pb-Pb age of 4561 ± 20 Ma (2σ, MSWD = 1.2).

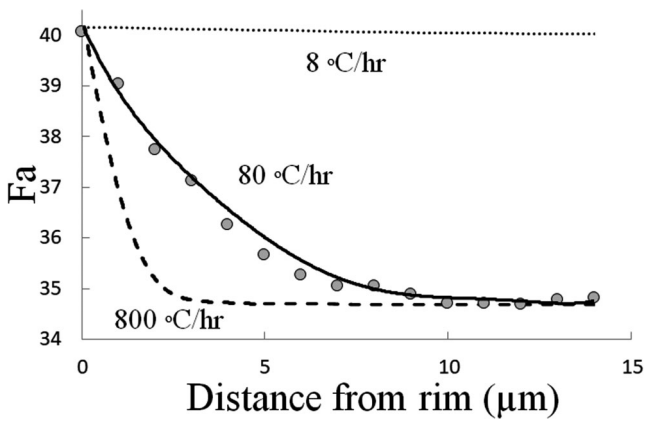

Fig. 12. Line profile of Fa# with 2 μm steps for the Fo_{64} olivine in NWA 7203, and the estimated zoning profiles for each cooling rate. We calculated atomic diffusion profiles for cooling from 1200 to 900 °C at log$f$O2 = IW + 2. The zoning profile estimated for a cooling rate of 80 °C h^{-1} matches best with the obtained Fa# line profiles of the Fo_{64} olivine.

grained lithologies, which is unique to this angrite. However, there are some quenched angrites whose textures are similar to either the fine-grained or coarse-grained lithologies in NWA 7203.

In terms of the fine-grained lithologies of NWA 7203, the textures of LEW 87051 and NWA 1670 are similar (Jambon et al., 2008; Mikouchi et al., 1996). Anorthite in these samples shows a lathy shape with parallel arrangement similar to a spinifex texture, and olivine and clinopyroxene fill the gap of elongated anorthite. However, anorthite in the groundmass of LEW 87051 is 30 μm × 1 mm in size whereas that in the groundmass of NWA 1670 is 20 μm × 500 μm. The size of anorthite in the fine-grained lithologies of NWA 7203 is smaller (mostly 5–10 μm × 20–100 μm). Furthermore, anorthite crystals in LEW 87051 and NWA 1670 are extremely elongated compared with that in NWA 7203 (Jambon et al., 2008; Mikouchi et al., 1996). The grain size of anorthite in NWA 1296 (around 10 μm × 40 μm) is as small as that in the fine-grained lithology of NWA 7203 (Jambon et al., 2005), but anorthite in NWA 1296 is always present as dendritic intergrowth with olivine and is texturally more similar to the coarse-grained lithology of NWA 7203.

The texture of the coarse-grained lithologies in NWA 7203 is most similar to those of NWA 1296, Sahara 99555, and D'Orbigny in the presence of olivine–anorthite intergrowth. The grain size of NWA 1296 (mostly around 40 μm, Jambon et al., 2005) is much smaller than that in coarse-grained lithologies of NWA 7203. Sahara 99555 shows a similar texture with coarse-grained lithologies of NWA 7203 and the grain size is also similar (around 500 μm, Mikouchi, McKay, Le, et al., 2000). However, there are euhedral olivine grains that do not show intergrowth with anorthite in Sahara 99555. D'Orbigny contains large mineral grains (~1 mm olivine and anorthite, and ~3mm clinopyroxene) equivalent to the grain size of coarse-grained lithologies in NWA 7203. However, dendritic intergrowth of olivine and anorthite is not common in D'Orbigny and, thus, these two meteorites are different.

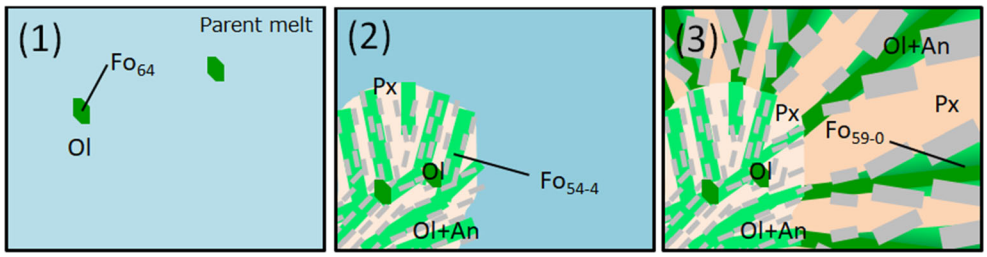

Fig. 13. Schematic illustration showing the crystallization process of NWA 7203. 1) Mg-rich olivine grains ($Fo_{\leq 64}$) crystallized in the parent melt. 2) Fine-grained variolitic texture rapidly crystallized with Mg-rich olivine grains as crystallization seeds at a relatively fast cooling rate (about 80 °C h^{-1}). 3) A new eruption of a lava flow buried this rock to a greater depth, resulting in a decrease in cooling rate to ~1 °C h^{-1}. Thus, final crystallization was completed at a slower cooling rate and produced a coarse-grained dendritic texture. (Color figure can be viewed at wileyonlinelibrary.com.)

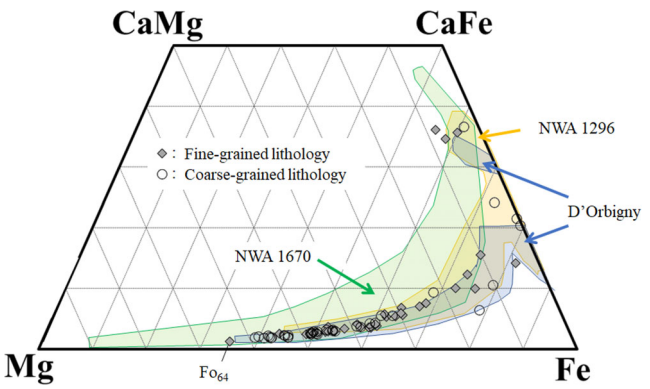

Fig. 14. Compositional range of olivine and kirschsteinite in NWA 7203 plotted on the Ca-Fe-Mg olivine quadrilateral. The chemical compositions of olivine in NWA 7203 are generally similar to those in NWA 1296 (Jambon et al., 2005), NWA 1670 (Jambon et al., 2008), and D'Orbigny (Mittlefehldt et al., 2002). (Color figure can be viewed at wileyonlinelibrary.com.)

The chemical composition of olivine in NWA 7203 is generally similar to those in NWA 1296, NWA 1670, and D'Orbigny although some differences exist. NWA 1296 olivine is clearly more Fe-rich (Jambon et al., 2005). NWA 1670 olivine is similar to NWA 7203 olivine in Fe-Mg composition, but is more Ca-rich (Jambon et al., 2008). D'Orbigny olivine is more Mg-rich than NWA 7203 olivine (Mittlefehldt et al., 2002) (Fig. 14).

The Ca-Fe-Mg composition of clinopyroxene in the coarse-grained lithologies of NWA 7203 is close to that of D'Orbigny (Mittlefehldt et al., 2002) and NWA 1296 (Jambon et al., 2005). Ca-Fe-Mg composition of clinopyroxene in fine-grained lithologies of NWA 7203 is similar to NWA 1670 (Jambon et al., 2008).

From the chemical composition of the most Mg-rich olivine phenocrysts in each sample, the Mg# of parent magmas increased in the following order: NWA 1670 > D'Orbigny ~ NWA 7203 > NWA 1296 (see Fig. 14). This Mg# depends on the amount of resorbed Mg-rich olivine xenocryst components incorporated into the parent melt (Mikouchi et al., 2004). In this case, it is possible that the original magma of these quenched angrites was the same, but the amount of incorporated Mg-rich olivine xenocrysts was different, resulting in the different Mg# of the parent melts.

Table 6 summarizes the estimated cooling rates and textural variations of quenched angrites. The cooling rate of NWA 7203 is considered to be around 80 °C h^{-1} for the fine-grained lithologies and ~1 °C h^{-1} for the coarse-grained lithologies. Cooling rates of quenched angrites that show lathy texture relatively similar to the fine-grained lithologies of NWA 7203 are 7–13 °C h^{-1} for LEW 87051 (Mikouchi et al., 2001) and 4 °C h^{-1} for NWA 1670 (Hayashi & Mikouchi, 2019). The cooling rate of Sahara 99555 that shows a dendritic texture similar to the coarse-grained lithologies of NWA 7203 is considered to be on the order of 1 °C h^{-1} (Mikouchi, McKay, & Le, 2000).

From cooling rates reported in this study and the literature, it appears that quenched angrites with rapid cooling rates show fine-grained and lathy textures, and those with relatively slow cooling rates show coarse-grained and ophitic or dendritic intergrowth textures. Each quenched angrite (except NWA 7203) has a single igneous texture, implying that the crystallization process of most quenched angrites was controlled by a simple cooling event. The observation that NWA 7203 shows two distinct textures (fine-grained lathy texture and coarse-grained dendritic texture) with a 1–2 mm transition zone suggests that NWA 7203 records cooling variations of a single eruption cycle in which a lobe of quenching basalt is overridden by a new breakout of lava from the main flow. However, such an event that resulted in a measurable change in cooling rates appears to have been rare on the APB.

Shock Metamorphism of NWA 7203

From optical microscopic observations, some minerals in or close to shock veins show undulose

Table 6. Relationship between textures and cooling rates of quenched angrites.

	NWA 7203 (coarse)	NWA 7203 (fine)	LEW 87051	Asuka-881371	Sahara 99555	D'Orbigny	NWA 1670
Grain length of anorthite	~1 mm	~100 μm	~1 mm	~1 mm	~500 μm	~500 μm	~500 μm
Texture	Dendritic	Variolitic, Lathy	Lathy	Ophitic	Dendritic	Ophitic	Lathy
Cooling rate (^{o}C h^{-1})	~1[a]	~80[a]	7–13[b]	7–13[b]	1[c]	7–13[b]	4[a]

[a]Hayashi and Mikouchi (2019) and this study.
[b]Mikouchi, McKay, and Le (2000).
[c]Mikouchi et al. (2001).

extinction. Some anorthite close to shock veins is amorphous, but anorthite is still crystalline in most parts. It has been experimentally determined that anorthite becomes amorphous (maskelynite) when shock pressure is over 20 GPa (Fritz et al., 2011; Stöffler et al., 1986). Thus, the shock pressure of NWA 7203 was under 20 GPa in most parts despite the presence of clear shock textures.

The only other known shocked quenched angrite is NWA 1670, which is typified by shock veins with a width of 30 μm. In some parts, pre-existing textures were displaced by up to 1 mm. Mikouchi et al. (2003) considered that mosaicism of olivine xenocrysts in NWA 1670 is the evidence for shock. Similarly, Jambon et al. (2008) considered mosaicked olivine xenocrysts as remnant of shock melting. The number and the size of shock veins in NWA 7203 are much larger than those of NWA 1670, and minerals in NWA 1670 show sharp extinction except for olivine xenocrysts, suggesting that shock metamorphism is stronger in NWA 7203 than in NWA 1670. Thus, NWA 7203 is the most shocked angrite.

The obtained Pb-Pb age of NWA 7203 is 4543 ± 19 Ma, but some spread in the data beyond analytical error probably indicates disturbance. This Pb-Pb age is not coincident with other quenched angrites (~4563 Ma, e.g., Amelin, 2008b; Schiller et al., 2015; Tissot & Dauphas, 2012; Zartman et al., 2006), suggesting that the Pb-Pb age of NWA 7203 was disturbed by the shock metamorphism. From this result, we conclude that NWA 7203 cannot be used as a time anchor such as other quenched angrites. Silico-apatites away (<200 μm) from shock veins have a Pb-Pb age of 4561 ± 20 Ma (coincident with other quenched angrites), which might imply that the Pb-Pb age was disturbed only near shock veins, and silico-apatites away from shock veins still retain a primary crystallization age.

According to Stöffler et al. (2018), 20 GPa shock for mafic rock will produce a 50–150 °C temperature rise of the whole rock. This is much lower than the closure temperature of the Pb-Pb age. However, shock veins exist in NWA 7203. In the shock veins, minerals melted and turned into glass during the shock event. This means that the temperature rose very high (~1400 °C) locally, where shock veins are present. Thus, in or near shock veins, the temperature was clearly higher than the closure temperature, resetting the Pb-Pb age, although most part of NWA 7203 experienced only 50–150 °C temperature rise, preserving the primary igneous Pb-Pb age.

Impacts and Evolutionary History of the APB

There are several studies discussing the size of the APB. Busemann et al. (2006) analyzed the composition of noble gases captured in D'Orbigny and found that $(^{20}Ne/^{22}Ne)_{tr}$ is 11.9 ± 0.3, which is similar to the solar composition. Although it is not clear whether the origin of noble gases is endogenic or exogenic to the APB, noble gases were trapped in the glass of quenched magma. From this result, they inferred the size of APB might have been 100–200 km in diameter. Weiss et al. (2008) studied magnetic fields recorded in Angra dos Reis, D'Orbigny, and Asuka-881371 whose ages are 4564–4558 Ma and found ~10 μT of magnetic fields, and they show the possibility that APB was larger than 150 km in diameter. Suzuki et al. (2014) estimated the upper limit of the diameter of APB to be 1400 ± 200 km by focusing on the spherical voids in D'Orbigny whose size depends on the gravity of APB. Therefore, the current best size estimate of the APB is 150–1600 km in diameter. Bogard (1995) suggested that the proportion of impacted or heated samples in meteorites increases with the size of parent body. Scott and Bottke (2011) provided two reasons for this—(1) a small body can lose materials more easily than a large body because of the small escape velocity and (2) the larger the size of a parent body, the more energy is needed to destroy the parent body (Asphaug, 2009), and the probability of such a collision is lower. Thus, Scott and Bottke (2011) argued that the angrite asteroids should have become small (<10 km in diameter) before the timing of the LHB and escaped shock

metamorphism during the LHB, in agreement with the observation that the majority of angrites have no shock textures. They propose that the APB was large (at least 100 km in diameter) and a major impact on it occurred ~4.5 Gyr ago, producing angritic asteroids. They argue that breccia formation and shock occurred predominantly after the destruction of their parent asteroids in family forming impacts, thus most angrites lack shock textures caused by the destruction.

However, 21 angrites have been found (as of October 2021) and NWA 1670 and NWA 7203 show clear evidence for shock metamorphism. Two of 21 is a significant proportion, which implies that shock metamorphism was more important in angrite asteroids than previously thought (Scott & Bottke, 2011). Some angrites might remain as one or more large asteroid (>10 km in diameter) during LHB. Alternatively, there is the possibility that angrites are indeed from small asteroids and most angrites escaped shock metamorphism, but some angrites suffered from local shock metamorphism.

Burbine et al. (2001) and Burbine et al. (2006) reported that the reflectance spectra of 289 Nenetta (37.6 km in diameter: Masiero et al., 2012) and 3819 Robinson (10.3 km in diameter: Masiero et al., 2012) showed relatively good agreement with that of D'Orbigny, suggesting that these asteroids can be one of the angrite asteroids, in agreement with our hypothesis of large angrite asteroids.

CONCLUSIONS

1. NWA 7203 shows two distinct textures whose grain sizes vary from fine (~10 μm) to coarse grained (~3 mm) in contrast to other quenched angrites that show single textures. Fine-grained lithologies show a variolitic texture while coarse-grained lithologies show a dendritic texture consisting of olivine and anorthite intergrowth, and clinopyroxene fills the gap of dendrites.
2. Unlike most angrites, NWA 7203 shows clear evidence for shock metamorphism. Anorthite close to shock veins becomes amorphous as indicated by broad Raman peaks, and in most parts, anorthites are still crystalline. From this observation, we infer that the shock pressure of NWA 7203 was under 20 GPa in spite of the presence of clear shock textures.
3. We measured Pb isotopic ratios of silico-apatites in NWA 7203. The Pb-Pb age of NWA 7203 is calculated to be 4543 ± 19 Ma, which is younger than other quenched angrites, but some scatter in the data beyond analytical error supports the interpretation of late disturbance. Silico-apatites away (<200 μm) from shock veins have a Pb-Pb age of 4561 ± 20 Ma (coincident with other quenched angrites), which might imply that the Pb-Pb age was disturbed only near shock veins, and silico-apatites away from shock veins still retain a primary crystallization age.
4. The bulk chemical composition of NWA 7203 is relatively Fe-rich compared with other quenched angrites, implying that the parent magma of NWA 7203 was relatively differentiated. This might depend on the amount of incorporated Mg-rich olivine xenocrysts (Mikouchi et al., 2004), and if this is the case, the amount of dissolved xenocryst component was not large for NWA 7203.
5. The cooling rate of NWA 7203 is estimated to be 80 °C h^{-1} in the fine-grained lithologies and ~1 °C h^{-1} in the coarse-grained lithologies, respectively. One of the possible scenarios to explain the change of cooling rates from fast to slow is that NWA 7203 records cooling variations of a single eruption cycle in which a lobe of quenching basalt is overridden by a new breakout of lava from the main flow. Alternatively, there is the possibility that changing cooling rates may simply be a function of cooling curve, such as before and after supercooling.
6. The finding of clear shock metamorphism of NWA 7203 suggests that some angrites might have remained as one or more large asteroids (>10 km in diameter) during LHB. Alternatively, it is possible that all angrites were derived from small asteroids (i.e., their immediate parents, not the original angrite parent body) and most angrites escaped shock metamorphism, but some angrites suffered from local shock metamorphism. Asteroids 289 Nenetta (37.6 km in diameter: Masiero et al., 2012) and 3819 Robinson (10.3 km in diameter: Masiero et al., 2012) are candidates for angritic asteroids.

Acknowledgments—Technical advice from Dr. N. Takahata for analysis of Pb isotopic ratios and discussion with Dr. T. Iizuka was helpful. We thank NIPR members for helping with Raman work and other observations of angrites. Mr. H. Yoshida and Mr. K. Ichimura supported electron microprobe work at Department of Earth and Planetary Science, the University of Tokyo. This study was supported by The Graduate Research Abroad in Science Program (GRASP2019-2), JSPS KAKENHI Grant Numbers 19H00726, 19H01959, and 21K18645, NIPR through General Collaboration Project no. 30-19 and KP307, GIMRT Program of the Institute for Materials Research, Tohoku University (Proposal No. 18K0006, 19K0024), the Astrobiology Center of National Institutes of Natural Sciences (NINS) (Grant Numbers

AB 31 1022 and AB 03 1004), and the KOPRI project (PE21050). M.B. acknowledges funding from the Carlsberg Foundation (CF18 1105) and the European Research Council (ERC Advanced Grant 833275-DEEPTIME). Detailed reviews by Drs. A. Zhang, S. McKibbin, and D. W. Mittlefehldt and editorial comments by Dr. C. A. Goodrich are gratefully acknowledged.

Data Availability Statement—The data that support the findings of this study are available upon reasonable request from the authors.

Editorial Handling—Dr. Cyrena Goodrich

REFERENCES

Amelin, Y. 2008a. U-Pb Ages of Angrites. *Geochimica et Cosmochimica Acta* 72: 221–32.

Amelin, Y. 2008b. The U-Pb Systematics of Angrite Sahara 99555. *Geochimica et Cosmochimica Acta* 72: 4874–85.

Asphaug, E. 2009. Growth and Evolution of Asteroids. *Annual Review of Earth and Planetary Sciences* 37: 413–48.

Bogard, D. D. 1995. Impact Ages of Meteorites: A Synthesis. *Meteoritics* 30: 244–68.

Brennecka, G. A., and Wadhwa, M. 2012. Uranium Isotope Compositions of the Basaltic Angrite Meteorites and the Chronological Implications for the Early Solar System. *Proceedings of the National Academy of Sciences* 109: 9299–303.

Burbine, T. H., McCoy, T. J., and Binzel, R. P. 2001. Spectra of Angrites and Possible Parent Bodies (Abstract #1857). 32nd Lunar and Planetary Science Conference. CD-ROM.

Burbine, T. H., McCoy, T. J., Hinrichs, J. L., and Binzel, R. P. 2006. Spectral Properties of Angrites. *Meteoritics & Planetary Science* 41: 1139–45.

Busemann, H., Lorenzetti, S., and Eugster, O. 2006. Noble Gases in D'Orbigny, Sahara 99555 and D'Orbigny Glass—Evidence for Early Planetary Processing on the Angrite Parent Body. *Geochimica et Cosmochimica Acta* 70: 5403–25.

Clayton, R. N., and Kieffer, S. W. 1991. Oxygen Isotopic Thermometer Calibrations. *Stable Isotope Geochemistry: A Tribute to Samuel Epstein*, edited by Tayor H. P., O'Neill J. R. and Kaplan I. R., 3–10. Washington DC: Geochemical Society.

Davidson, P. M., and Mukhopadhyay, D. K. 1984. Ca-Fe-Mg Olivines: Phase Relations and a Solution Model. *Contributions to Mineralogy and Petrology* 86: 256–63.

Fritz, J., Wünnemann, K., Greshake, A., and Fernandes, V. A. 2011. Shock Pressure Calibration for Lunar Plagioclase (Abstract #1196). 42nd Lunar and Planetary Science Conference. CD-ROM.

Greenwood, R. C., Franchi, I. A., Jambon, A., and Buchanan, P. C. 2005. Widespread Magma Oceans on Asteroidal Bodies in the Early Solar System. *Nature* 435: 916–8.

Hayashi, H., and Mikouchi, T. 2019. On the Relationship Between Textures and Cooling Rates of Quenched Angrites. The 10th Symposium on Polar Science, OA-116.

Hayashi, H., Takenouchi, A., Mikouchi, T., and Bizzarro, M. 2018. Shock Metamorphism of the Northwest Africa 7203 Angrite (Abstract #1932). 49th Lunar and Planetary Science Conference. CD-ROM.

Jambon, A., Barrat, J. A., Boudouma, O., Fonteilles, M., Badia, D., Göpel, C., and Bohn, M. 2005. Mineralogy and Petrology of the Angrite Northwest Africa 1296. *Meteoritics & Planetary Science* 40: 361–75.

Jambon, A., Omar, B., Michel, F., Guillou, L. E., Badia, D., and Barrat, J. A. 2008. Petrology and Mineralogy of the Angrite Northwest Africa 1670. *Meteoritics & Planetary Science* 43: 1783–95.

Jurewicz, A. J. G., Mittlefehldt, D. W., and Jones, J. H. 1993. Experimental Partial Melting of the Allende (CV) and Murchison (CM) Chondrites and the Origin of Asteroidal Basalts. *Geochimica et Cosmochimica Acta* 57: 2123–39.

Keil, K. 2012. Angrites, a Small But Diverse Suite of Ancient, Silica-Undersaturated Volcanic-Plutonic Mafic Meteorites, and the History of Their Parent Asteroid. *Chemie der Erde—Geochemistry* 72: 191–218.

Kim, N. K., Kusakabe, M., Park, C., Lee, J. I., Nagao, K., Enokido, Y., Yamashita, S., and Park, S. Y. 2019. An Automated Laser Fluorination Technique for High-Precision Analysis of Three Oxygen Isotopes in Silicates. *Rapid Communications in Mass Spectrometry* 33: 641–9.

Kim, N. K., Park, C., and Kusakabe, M. 2020. Two-Point Normalization for Reducing Inter-Laboratory Discrepancies in $\delta^{17}O$, $\delta^{18}O$, and $\Delta'^{17}O$ of Reference Silicates. *Journal of Analytical Science and Technology* 11: 51.

Kleine, T., Hans, U., Irving, A. J., and Bourdon, B. 2012. Chronology of the Angrite Parent Body and Implications for Core Formation in Protoplanets. *Geochimica et Cosmochimica Acta* 84: 186–203.

Koike, M., Ota, Y., Sano, Y., Takahata, N., and Sugiura, N. 2014. High-Spatial Resolution U-Pb Dating of Phosphate Minerals in Martian Meteorite Allan Hills 84001. *Geochemical Journal* 48: 423–31.

Longhi, J. 1999. Phase Equilibrium Constraints on Angrite Petrogenesis. *Geochimica et Cosmochimica Acta* 63: 573–85.

Ma, C., and Beckett, J. R. 2017. A New Type of Tissintite, (Ca, Mg, Na,□0.14)(Al, Fe, Mg)Si2O6, in the Zagami Martian Meteorite: A High-Pressure Clinopyroxene Formed by Shock (Abstract #1639). 48th Lunar and Planetary Science Conference. CD-ROM.

Masiero, J. H., Mainzer, A. K., Grav, T., Bauer, J. M., Cutri, R. M., Nugent, C., and Cabrera, M. S. 2012. Preliminary Analysis of *WISE*/NEOEISE 3-Band Cryogenic and Post-Cryogenic Observations of Main Belt Asteroids. *The Astrophysical Journal Letters* 759: L8.

McKeegan, K. D., and Davis, A. M. 2003. Early Solar System Chronology. *Treatise on Geochemistry* 1: 431–60.

Meteoritical Bulletin Database. https://www.lpi.usra.edu/meteor/metbull.php.

Mikouchi, T., and Bizzarro, M. 2012. Mineralogy and Petrology of NWA 7203: A New Quenched Angrite Similar to NWA 1296 and NWA 1670. *Meteoritics & Planetary Science* 47(Supplement): 5120.

Mikouchi, T., McKay, G., and Jones, J. H. 2004. Sahara 99555 and D'Orbigny: Possible Pristine Parent Magma of Quenched Angrites (Abstract #1504). 35th Lunar and Planetary Science Conference. CD-ROM.

Mikouchi, T., McKay, G., Koizumi, E., Monkawa, A., and Miyamoto, M. 2003. Northwest Africa 1670: A New

Quenched Angrite. *Meteoritics & Planetary Science* 38 (Supplement): A115.

Mikouchi, T., McKay, G., and Le, L. 1994. Cr, Mn and Ca Distributions for Olivine in Angritic Systems: Constraints on the Origins of Cr-Rich and Ca-Poor Core Olivine in Angrite LEW87051 (Abstract). 25th Lunar and Planetary Science Conference. p. 907.

Mikouchi, T., McKay, G., and Le, L. 2000. Experimental Crystallization of the Asuka-881371 (Angrite) Groundmass Composition: Implication for Crystallization Histories of Sahara 99555. *Meteoritics & Planetary Science* 35 (Supplement): A110–1.

Mikouchi, T., McKay, G., Le, L., and Mittlefehldt, D. W. 2000. Preliminary Examination of Sahara 99555: Mineralogy and Experimental Study of a New Angrite (Abstract #1970). 31st Lunar and Planetary Science Conference. CD-ROM.

Mikouchi, T., Miyamoto, M., and McKay, G. 1996. Mineralogical Study of Angrite Asuka-881371: Its Possible Relation to Angrite LEW 87051. *Proceedings of the NIPR Symposium on Antarctic Meteorites* 9: 174–88.

Mikouchi, T., Miyamoto, M., McKay, G., and Le, L. 2001. Cooling Rate Estimates of quenched Angrites: Approaches by Crystallization Experiments and Cooling Rate Calculations of Olivine Xenocrysts. *Meteoritics & Planetary Science* 36(Supplement): A134–5.

Mittlefehldt, D. W., Killgore, M., and Lee, M. T. 2002. Petrology and Geochemistry of D'Orbigny, Geochemistry of Sahara 99555, and the Origin of Angrites. *Meteoritics & Planetary Science* 37: 345–369.

Misener, D. J. 1974. Cationic Diffusion in Olivine to 1400 °C and 35 kbar. *Geochemical Transport and Kinetics* 634: 117–29.

Miyamoto, M., Mikouchi, T., and Arai, T. 2002. Comparison of Fe-Mg Interdiffusion Coefficients in Olivine. *Antarctic Meteorite Research* 15: 143–51.

Roeder, P. L., and Emslie, R. F. 1970. Olivine-Liquid Equilibrium. *Contributions to Mineralogy and Petrology* 29: 275–89.

Schiller, M., Connelly, J. N., Glad, A. C., Mikouchi, T., and Bizzarro, M. 2015. Early Accretion of Protoplanets Inferred from a Reduced Inner Solar System ^{26}Al Inventory. *Earth and Planetary Science Letters* 420: 45–54.

Scott, E. R. D., and Bottke, W. F. 2011. Impact Histories of Angrites, Eucrites, and Their Parent Bodies. *Meteoritics & Planetary Science* 46: 1878–87.

Stöffler, D., Hamann, C., and Metzler, K. 2018. Shock Metamorphism of Planetary Silicate Rocks and Sediments: Proposal for an Updated Classification System. *Meteoritics & Planetary Science* 53: 5–49.

Stöffler, D., Ostertag, R., Jammes, C., Pfannschmidt, G., Gupta, P. R. S., Simon, S. B., Papike, J. J., and Beauchamp, R. H. 1986. Shock Metamorphism and Petrography of the Shergotty Achondrite. *Geochimica et Cosmochimica Acta* 50: 889–903.

Suzuki, H., Ozawa, K., Nagahara, H., and Mikouchi, T. 2014. Estimate of Radius Size of the Angrite Parent Body (in Japanese). 2014 Annual Meeting of Japan Geoscience Union. PPS22-04.

Tissot, F. L. H., and Dauphas, N. 2012. 238U/235U Ratios of Anagrams: Angrites and Granites (Abstract #1981). 43rd Lunar and Planetary Science Conference. CD-ROM.

Weiss, B. P., Berdahl, J. S., Ekins-Tanton, L., Stanley, S., Lima, E. A., and Carporzen, L. 2008. Magnetism on the Angrite Parent Body and the Early Differentiation of Planetesimals. *Science* 31: 713–6.

Zartman, R. E., Jagoutz, E., and Bowring, S. A. 2006. Pb-Pb Dating of the D'Orbigny and Asuka 881371 Angrites and a Second Absolute Time Calibration of the Mn-Cr Chronometer (Abstract #1580). 37th Lunar and Planetary Science Conference. CD-ROM.